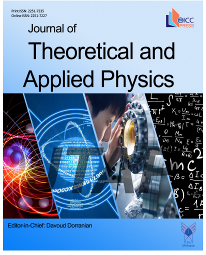

Volume 19, Issue 5, 192543 (1-17)

Journal of Theoretical and Applied Physics (JTAP)

https://doi.org/10.57647/j.jtap.2025.1905.43

Optimizing reaction time in hydrothermal synthesis of nanocomposites V_2O_5/PANI for improved photodetector applications performance

Tayba Abd Allatife Ibrahim[1,*], Ahmed S Obaid Alqayssei[1,2,*], Ibraheem J. Ibraheem[3]

[1] *Department of Physics, College of Science, University of Anbar, Ramadi, Iraq.*
[2] *Nanomaterials Research Center, University of Anbar, Ramadi, Iraq.*
[3] *Department of Chemistry, College of Science, University of Anbar, Ramadi, Iraq.*

***Corresponding authors:** tib22s2003@uoanbar.edu.iq, sc.ahmed.s.obaid.alqayssei@uoanbar.edu.iq

Original Research
Received:
14 March 2025
Revised:
12 July 2025
Accepted:
22 August 2025

Abstract:

This study assesses the photodetection efficacy of a nanocomposite heterojunction photodetector utilizing V_2O_5, PANI, and V_2O_5/PANI thin films. The nanocomposites were manufactured by a hydrothermal approach for 6 and 8 hours, then coated onto silicon (Si) substrates using a spray-coating technique. X-ray diffraction (XRD) examination verified the orthorhombic crystalline structure of V_2O_5 and the semi-crystalline characteristics of PANI. The nanocomposite synthesis led to noticeable alterations in both structures, with the reaction duration markedly affecting the crystallinity. Raman spectroscopy identified unique vibrational modes for each component, and the composite spectra exhibited distinctive changes indicative of robust molecular interactions. FESEM and AFM investigations revealed improved surface texture and suitable roughness in the sample synthesized at 6 hours and 180 °C, facilitating optimal morphology for effective photocarrier production and transport. Photoluminescence (PL) experiments verified that the active spectrum response of the nanocomposite photodetector ranges from 300 to 700 nm. The device constructed with a 6-hour response time demonstrated optimum performance, with a responsivity of 0.383 μA/W, a detectivity of 1.77×10^{20} Jones, and an external quantum efficiency of 153.2% at a 2 V bias and 10 mW/cm^2 light intensity. The reaction and recovery durations were 0.62 and 0.59 seconds, respectively. The results indicate the structural and functional dependability of the V_2O_5/PANI nanocomposite, presenting a viable avenue for constructing efficient optoelectronic devices.

Keywords: Hydrothermal; Time rection; Nanocomposite; Visible light photodetector; V_2O_5/PANI; Spray coting

1. Introduction

Recently, there has been significant interest in microelectronic and optoelectronic devices utilizing vanadium pentoxide (V_2O_5), a crucial transition-metal oxide semiconductor [1]. V_2O_5 is a potential material for photodetection applications owing to its direct bandgap in the visible-light spectrum ($E_g = 2.2 - 2.9$ eV) and its classification as an n-type metal oxide semiconductor [2]. Crystalline V_2O_5 exhibits a distinctive orthorhombic layered structure, a direct optical energy gap, advantageous chemical stability, thermal resistance, and elevated specific energy [3]. These characteristics render it appealing for several applications, such as solar cell windows, catalysts [4], infrared detectors [5], gas sensors [6], and optoelectronic devices [7]. Despite its outstanding photovoltaic properties, V_2O_5 has comparatively worse electrical conductivity and an elevated electron-hole recombination rate in comparison to other conductive substances. Consequently, the amalgamation of V_2O_5 with additional components is frequently essential to augment its efficacy in practical applications [8]. The primary function of a photodetector is to produce electron-hole pairs in response to input light; hence, the photovoltaic performance of V_2O_5 can be enhanced by integrating nanoscale elements into its matrix to customize its features for particular applications. Polyaniline (PANI), in its emeraldine salt form, stands out among traditional conducting polymers. It has a wide range of desirable properties, such as being sensitive to visible light (bandgap: $2.5-3$ eV), being easily synthesized at a low cost, being redox tunable via acid/base doping, having adjustable conductivity, and being environmentally stable [9–12]. Nanoscale materials embedded in a polymer matrix to make polymeric nanocomposites have found extensive application in performance enhancement. Composites made of PANI have been engineered using a wide range of additives, including organic molecules, carbon nanostructures, metal oxides, and other polymers [13]. To add to its sensitivity in the visible-light spectrum, PANI exhibits a HOMO-LUMO energy gap below 2.8 eV [14, 15]. So, a V_2O_5/PANI heterojunction could be a good choice for developing multicolor photodetectors (PDs) since it could provide novel optoelectronic features neither material could provide. Flexible V_2O_5/PANI heterojunctions for UV and visible light detection have not been described in any prior investigations as far as we are aware. Here, we detail the process of creating and studying V_2O_5/PANI heterojunctions that can detect many colors when exposed to ultraviolet and visible light. The electrical and optical characteristics of the suggested devices were examined by measuring the current voltage (I-V) and analyzing the photocurrent response.

2. Experimental

2.1 Materials

The materials such as aniline (99.9%) monomer, ammonium persulfate (APS), hydrochloric acid (HCl), ammonium metavanadate (NH_4VO_3) ethanol and deionized water were purchased from sigma Aldrich.

2.2 Synthesis of PANI

Polyaniline (PANI) in its emeraldine salt (ES) form was created using chemical oxidative polymerization of aniline in an acidic environment. The synthesis entailed the formulation of two distinct solutions: Solution 1 comprised 10 mL of hydrochloric acid (HCl), 20 mL of deionized water, and 3 mL of aniline; Solution 2 included 4 g of ammonium persulfate (APS) mixed in 30 mL of deionized water.

After 40 minutes of individual agitation, Solution 2 was incrementally introduced to Solution 1 while maintaining continuous stirring. A progressive color transition from blue to dark green was noted, signifying the synthesis of PANI by oxidative polymerization. The reaction mixture was stirred for another 3 hours to finalize the polymerization process. The green precipitate of PANI was recovered via filtering, extensively rinsed with deionized water to eliminate contaminants, and dried in an oven at 60 °C for 6 hours.

2.3 Synthesis of V_2O_5

Vanadium pentoxide (V_2O_5) nanostructures were produced through the thermal breakdown of 2 g of ammonium metavanadate (NH_4VO_3) in a sealed autoclave at a temperature range of $500-550$ °C for 2 hours. During breakdown, water and ammonia gasses were generated as byproducts and evaporated due to the high temperature, as indicated by the following reaction:

$$2NH_2VO_3 \xrightarrow{500\text{-}550\ ^\circ C} V_2O_5 + H_2O + 2NH_3 \qquad (1)$$

Following thermal treatment, the resultant V_2O_5 powder was solubilized in deionized water to provide a concentrated working solution, which was then utilized to synthesize the nanocomposite.

2.4 Synthesis of V_2O_5/PANI nanocomposites

V_2O_5/PANI nanocomposites were manufactured via a straightforward, economical, surfactant-free hydrothermal technique. Two samples, VP-6h and VP-8h, were produced with an identical weight ratio 1:3 (V_2O_5:PANI). Precisely, 0.125 g of V_2O_5 powder and 0.375 g of polyaniline (PANI) were allocated into individual tubes. Each tube received 25 mL of deionized water, followed by ultrasonic treatment for 25 minutes to achieve uniform dispersion of the components.

After ultrasonication, each combination was placed into a Teflon-lined stainless-steel autoclave for hydrothermal processing. The VP-6h sample was heated in an oven at 180 °C for 6 hours, whereas the VP-8h sample underwent identical conditions for 8 hours. After the heat procedure, the autoclaves were allowed to cool naturally to ambient temperature, and the resultant nanocomposites were gathered for further examination.

2.5 Fabrication of the photodetector device

Nanocomposites V_2O_5/PANI were deposited onto p-type silicon substrates to fabricate the photodetector device. Before deposition, the substrates underwent a comprehensive cleaning process involving sequential cleaning with deionized water, acetone, and ethanol, in addition to one hour of sonication in a water bath to eliminate dust, fingerprints, and residual surface contaminants. The substrates were then dried with a nitrogen gas stream. Nanocomposite films were deposited using spray-coating techniques. As shown in (figure 1), the cleaned silicon substrates were positioned on a hot plate from 80 °C to 85 °C. 50 spray cycles were conducted, each lasting 5 seconds and a 25-second interval for drying between consecutive sprays. This technique facilitated the creation of uniform thin films with thicknesses that varied according to the parameters of the spray application.

Moderately thick films are generally ideal for photodetector applications, as they effectively balance electrical conductivity and light absorption, ensuring sufficient charge carrier mobility while facilitating adequate interaction with incident photons to produce electron-hole pairs. Conversely, skinny films generally demonstrate increased electrical conductivity owing to reduced carrier transport distances; however, they may exhibit diminished light absorption, leading to lower photocurrent and elevated noise levels. Excessively thick films can absorb significant amounts of light and generate more photogenerated carriers. However, this may increase recombination rates and diminished carrier collection efficiency, attributed to longer transport distances and elevated bulk resistance [16]. Following film deposition, silver electrodes were applied to the surface of the nanocomposite-coated substrates through an electrodeposition technique, thus finalizing the fabrication of the photodetector device.

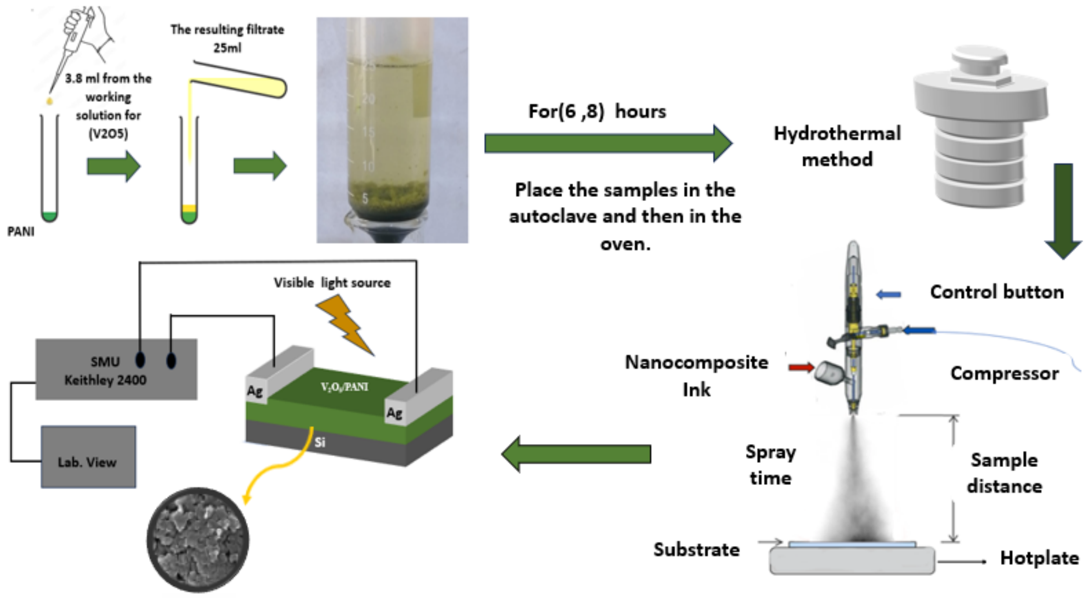

Figure 1. The experimental steps for preparation of V_2O_5, PANI and V_2O_5/PANI nanocomposite thin films and fabrication processes photodetector.

2.6 Characterization techniques

Several techniques were employed to characterize the V_2O_5, PANI, and V_2O_5/PANI nanocomposites. The structural investigation of nanoparticles was done by applying a Shimadzu-6000 X-ray apparatus. The gadget used a Cu-Kα radiation source at 0.15406 nm. The operational current was 40 mA at 40 kV. The samples were scanned from 5 to 70 degrees. The study utilized an advanced Field Emission Scanning Electron Microscope (FESEM) from ARYA Electron Optic, equipped with energy-dispersive X-ray (EDX) capabilities. This device provides elemental and topographical data with significantly enhanced image clarity, reduced electrostatic distortion, and three to six times higher resolution than traditional SEMs. Using an AFM, the nanoparticles' topography, surface morphology, and particle size distribution were examined (Mountains SPIP Expert 8.2.9621). This phenomenon is used to examine the energy structure of semiconductor materials. With an excitation wavelength of 320 nm, the FS-1401004 instrument was utilized to detect photoluminescence within a scanning range of 350 to 700 nm. Using a Horiba JOBIN YVON HR800, the Raman spectra were examined. To analyze the bonding structure, a (SUNSHINE-V2-86) device was used to measure the Raman spectrum. Finally, the I–V characteristics of the fabricated based-visible light photodetectors were analyzed via Keithley 237 SMU with 10 s on/off switching period and variety of illumination power intensity (AM 1.5 G filter).

3. Results and discussion

3.1 Structural analysis

X-ray diffraction (XRD) analysis was utilized to examine the crystallinity, phase composition, and structural evolution of as-deposited V_2O_5, polyaniline (PANI), and V_2O_5/PANI nanocomposite thin films synthesized through spray coating on silicon substrates. Figure 2 (a) illustrates the XRD pattern of pure V_2O_5, showcasing notable diffraction peaks at $2\theta = 15.3°$, $20.3°$, $21.7°$, $26.9°$, $31.1°$, and $41.2°$, which align with the (200), (001), (101), (110), (400), and (002) crystallographic planes, respectively. The observed peaks correspond to the orthorhombic phase of V_2O_5 (JCPDS 00-009-0387) [17], with the prominent (101) reflection highlighting its layered structure, which is essential for the improvement of semiconducting properties. The distinct, impurity-free peaks affirm a high degree of crystallinity and phase purity, aligning with the principles of thermal decomposition synthesis.

Conversely, figure 2 (b) exhibits a broad peak of PANI centered at $2\theta = 23.16°$, which is ascribed to scattering from semi-crystalline polyaniline chains alongside a low-angle feature ($2\theta = 6.0 - 10°$) peaking at 9.25°, suggesting the presence of ordered PANI chains in the emeraldine salt form. As previously documented, the semi-crystalline behavior emerges from oxidative polymerization conducted in acidic media without cooling [18, 19].

The V_2O_5/PANI nanocomposites figure 2 (c), synthesized over reaction durations of 6 h (VP-6h) and 8 h (VP-8h), demonstrate structural alterations attributed to the intercalation of PANI and the redox processes involving vanadium. VP-6h maintains the principal orthorhombic V_2O_5 peaks, albeit with diminished intensity, and exhibits two broadened PANI peaks, in addition to novel (00l) reflections at $2\theta \approx 8.38°$ corresponding to monoclinic VO_2 (JCPDS 01-071-0288) [20]. This indicates an expansion of the interlayer spacing from 0.43 nm in pristine V_2O_5 to 1.42 nm, thereby confirming the intercalation of PANI into the (002) planes. The VP-8h sample exhibits additional structural changes, characterized by a reduction in V_2O_5 peak intensity, significant broadening of the PANI peak, and a faint monoclinic VO_2 peak at $2\theta = 38.13°$. The observed alterations indicate an extended reaction-driven reduction of vanadium ($V^{+5} \rightarrow V^{+4}$) alongside lattice strain, wherein V^{+4} ions facilitate the polymerization of PANI and contribute to the stabilization of intercalated H_2O-V_2O_5-PANI structures [21].

The quantitative analysis of crystallography, as presented in

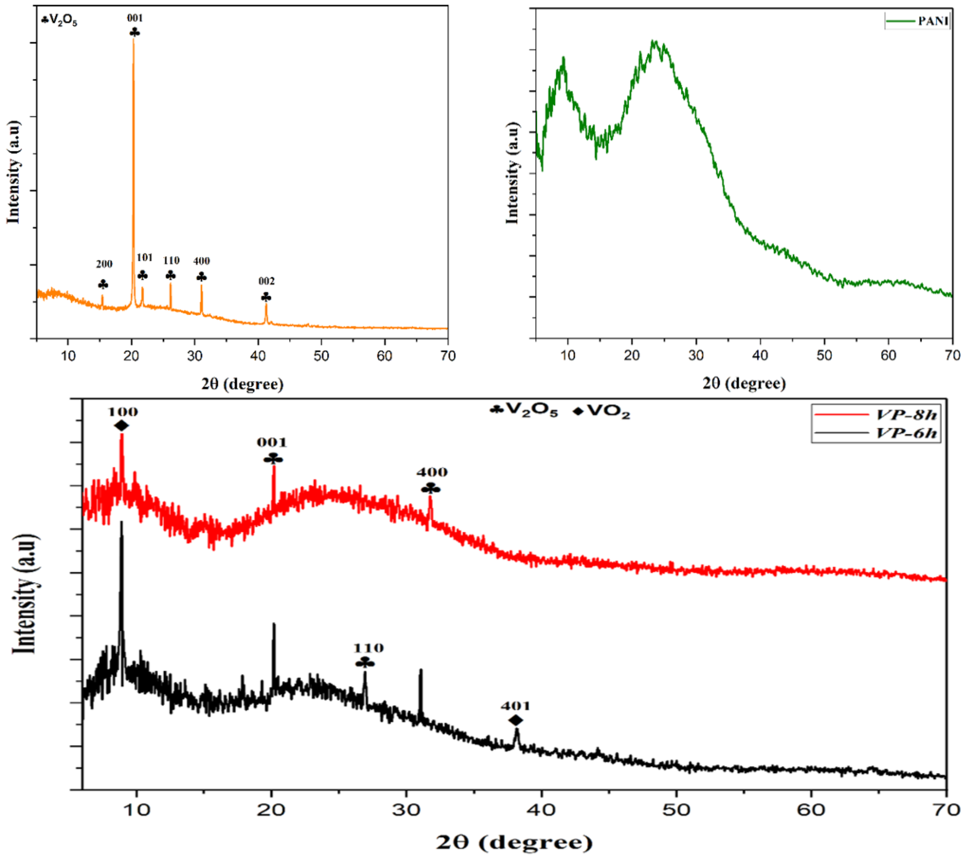

Figure 2. XRD patterns of (a) V_2O_5,(b) PANI, and (c) nanocomposite V_2O_5/PANI thin films synthesized with reaction times of 6 hours and 8 hours.

Table 1, employs Scherrer's equation (the crystalline size), dislocation density, and macro strains were obtained by applying equations (2), (3), and (4), respectively [22, 23]:

$$D = \frac{0.9\lambda}{\beta\cos\theta} \tag{2}$$

$$\delta = \frac{1}{D^2} \tag{3}$$

$$\eta = \frac{\beta}{4\tan\theta} \tag{4}$$

where D is the crystallite size, K is the form factor (often 0.9), λ is the X-ray wavelength (1.5406 Å for Cu $K\alpha$), β is the full width at half maximum (FWHM) of the diffraction peak in radians, and θ is the Bragg angle.

Elucidating notable trends. Pristine V_2O_5 demonstrates crystallite dimensions ranging from 35.5 to 111.6 nm, with dislocation densities between 0.07 and 0.80×10^{-3} nm^{-2}, alongside microstrains varying from 1.34 to 5.01×10^{-3} nm^{-1}, indicative of a moderate degree of lattice distortion. VP-6h exhibits diminished crystallite dimensions (61.3 nm for monoclinic VO_2) and an increased dislocation density (0.27×10^{-3} nm^{-2}), indicating structural perturbation due to PANI intercalation. VP-8h exhibits additional crystallite refinement (27.5 nm for VO_2) and an increase in defects, as evidenced by dislocation density and microstrain values of 1.33×10^{-3} nm^{-2} and 17.65×10^{-3} nm^{-1}, respectively. This phenomenon can be linked to the prolonged reaction time, which facilitates vanadium reduction and contributes to lattice disorder. The observed trends support the transition from orthorhombic to monoclinic phases, which is influenced by redox interactions occurring during the polymerization of PANI [24]. The heightened microstrain in VP-8h corresponds with similar oxide-polymer systems, wherein extended synthesis intensifies lattice distortion [25]. The intercalation mechanism, driven by V^{4+} ions and the resulting expansion of interlayer spacing, facilitates the customization of structural and electronic properties in V_2O_5/PANI nanocomposites, thereby establishing them as noteworthy contenders for semiconductor applications.

3.2 Raman spectroscopy analysis

Figure 3 displays Raman spectroscopy of vanadium pentavalent oxide (V_2O_5), polyaniline (PANI), and the hydrothermally synthesized V_2O_5/PANI nanocomposite exhibited unique spectrum fingerprints indicative of the structural and molecular interactions among the constituents. Figure 3 (a) distinct peaks for V_2O_5 were 103, 148, 308, 360, 512, 590, 695, 780, 940, and 1073 cm^{-1}. Lower peaks (< 400 cm^{-1}) signify lattice vibrations and bending of V-O-V bonds, whereas the $500-700$ cm^{-1} range corresponds to in-plane vibrations related to bond coordination in the orthorhombic structure [26]. The peak at 940 cm^{-1} indicates the V=O terminal bond stretching, signifying the level of crystallinity and the existence of highly symmetric terminal bonds [27, 28]. The high-frequency Raman signal at around 1073 cm^{-1} corresponds to the vanadyl oxygen stretching mode (V=OV) [29]. The observed splitting probably results

Table 1. Shows 2θ, full width at half maximum, crystal size, dislocation density, micro strains of V_2O_5 and V_2O_5/PANI (VP-6h, VP-8h).

Code sample	2θ	FWHM	Miller indices	Crystalline size (nm)	Dislocation density (δ) $\times 10^{-3}$	Micro strains (nm^{-2}) $\times 10^{-3}$	Crystal system	Chemical formula
V_2O_5	15.3	0.143	2 0 0	56.05	0.3182	4.64	Orthorhombic	V_2O_5
	20.3	0.094	0 0 1	85.85	0.135	2.29	Orthorhombic	V_2O_5
	21.7	0.22	1 0 1	36.76	0.73	5.008	Orthorhombic	V_2O_5
	26.1	0.23	1 1 0	35.45	0.79	4.32	Orthorhombic	V_2O_5
	31.1	0.173	4 0 0	47.66	0.44	2.71	Orthorhombic	V_2O_5
	41.2	0.086	0 0 2	35.45	0.79	4.32	Orthorhombic	V_2O_5
Vp-6h	8.2	0.13	1 0 0	61.29	0.26	7.37	Monoclinic	VO_2
	20.2	0.135	0 0 1	59.77	0.27	3.30	Orthorhombic	V_2O_5
	26.9	0.0732	1 1 0	111.58	0.08	1.33	Orthorhombic	V_2O_5
	31.1	0.067	4 0 0	123.07	0.06	1.051	Orthorhombic	V_2O_5
	38.1	0.1282	4 0 1	65.56	0.232	1.61	Orthorhombic	V_2O_5
Vp-8h	8.2	0.29	1 0 0	27.46	1.32	17.65	Monoclinic	VO_2
	20.2	0.123	1 1 0	65.46	0.233	3.013	Orthorhombic	V_2O_5
	31.7	0.25	4 0 0	32.94	0.92	3.84	Orthorhombic	V_2O_5

from local structural distortions or fluctuations in the bonding environment inside the V_2O_5 lattice.

Figure 3 (b) exhibits the polyaniline spectra displayed significant peaks at 447, 512, 587, 705, 762, 876, 965, 1065, 1194, 1275, 1321, 1480, 1562, and 1605 cm^{-1}, indicative of the polymer chain structure in the semi-oxidized state (emeraldine salt) [30, 31]. The peaks at $447 - 762$ cm^{-1} result from C–H wagging and C–N–C bending vibrations, but the peaks at $876 - 1065$ cm^{-1} signify out-of-plane ring vibrations, demonstrating the uniformity of the polymer chain. The peaks at $1194 - 1321$ cm^{-1} correspond to C–N and C=N vibrations, indicative of polaron-type local charges, whereas the peaks at $1480 - 1605$ cm^{-1} signify C=C stretching in the aromatic rings, which are linked to the oxidation state and electrical conductivity within the chain [32, 33].

Figure 3 (c) illustrates the amalgamation of V_2O_5 and PANI by hydrothermal treatment resulted in a nanocomposite that displayed a characteristic spectrum, indicating a structural interaction between the two substances, with peaks seen at 110, 147, 360, 470, 587, 695, 775, 870, 940, 1075, 1200, 1262, 1321, 1502, and 1569 cm^{-1}. The existence of peaks characteristic of V_2O_5 (e.g., 310, 360, 940 cm^{-1}) signifies partial preservation of the crystalline architecture of the inorganic component, whereas the peaks linked to PANI (587, 695, 1262, 1321, 1502, 1569 cm^{-1}) denote successful interpenetration of the polymer chains within the crystalline framework. Moreover, supplementary peaks were detected at 310 and 508 cm^{-1} in the nanocomposite, ascribed to a secondary phase of vanadium oxide, VO_2, in the monoclinic configuration. These peaks signify distinct vibrations of the VO_2 structure, contrasting with those of V_2O_5, showing the emergence of minor quantities of this phase due to the hydrothermal environment's heat and pressure reaction conditions. This transition signifies a change in oxidation state from V^{5+} to V^{4+}, influencing the electrical and structural characteristics of the composite [34, 35]. Upon comparison of the two samples with varying reaction periods (6 and 8 hours), the VP-6h sample exhibits sharper and more distinct peaks, signifying a greater degree of crystallinity and enhanced structural regularity. The VP-8h sample subjected to an extended reaction duration (8 hours) demonstrates minor blue changes towards elevated frequencies at the peaks of 870, 940, 1075, 1200, 1262, 1321, 1502, and 1569 cm^{-1}. The observed shifts can be attributed to the prolonged reaction time, which facilitates chemical bond rearrangements and enhances interlocking between the PANI chains and vanadium ions, resulting in bond shortening (notably V=O and C=N bonds) and an elevation in their vibrational energy [36], manifesting spectrally as a shift toward higher values [37]. Moreover, prolonged excessive reaction may result in the formation of secondary crystals or irregular partial recrystallization, diminishing the purity of the parent structure and impacting the Raman spectrum. From a chemical standpoint, the ideal reaction duration (6 hours) establishes an equilibrium between the rate of crystal growth and the development of interfacial bonds between V_2O_5 and PANI while avoiding “interfacial saturation” that may result in adverse compositional alterations. From a physical standpoint, preserving nanoscale dimensions and uniform distribution of components in a reduced timeframe improves the clarity of spectral peaks and diminishes the impact of random structural interference, resulting in enhanced electrical and

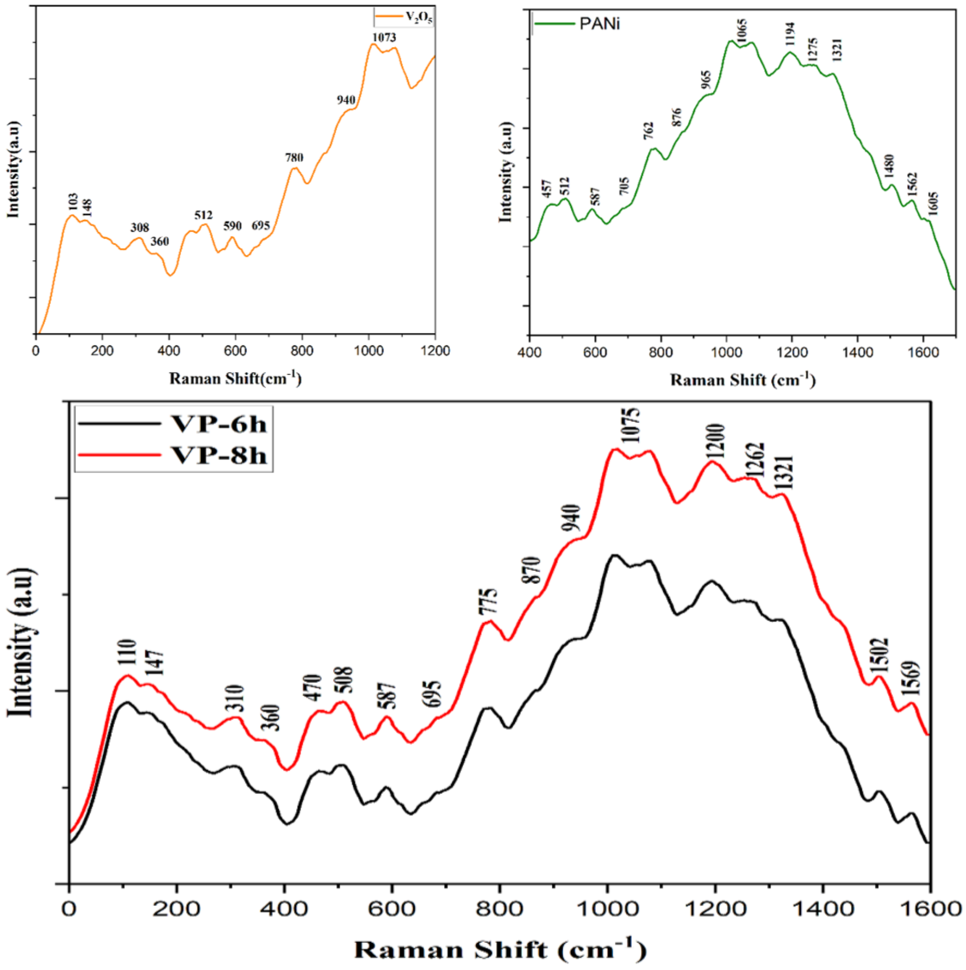

Figure 3. Raman spectroscopy of (a) V_2O_5, (b) PANI, and (c) V_2O_5/PANI synthesized with reaction times of 6 hours and 8 hours.

optical properties due to the facilitation of charge transfer within a more orderly structure [38].

3.3 Field emission scanning electron microscopy (FE-SEM) and EDX

The surface morphology of vanadium pentoxide (V_2O_5), polyaniline (PANI), and their nanocomposites were examined using field-emission scanning electron microscopy (FE-SEM), as seen in figure 4. Pure PANI (figure 4 a) has a fibrous and foamy morphology with considerable porosity, marked by a rough surface that improves its detection efficacy by auguring active sits [39]. Energy-dispersive X-ray (EDX) examination verifies the elemental composition, revealing atomic percentages of carbon (C) at 83.91% and nitrogen (N) at 16.09%, consistent with the polymer's organic backbone. Conversely, V_2O_5 (figure 4 b) exhibits a hybrid morphology of nanorods and nanosheets, dictated by the synthesis temperature, characterized by a uniform surface and EDX-derived atomic percentages of vanadium (V) and oxygen (O) at 29.17% and 70.83%, respectively, aligning with its stoichiometric composition [25].

The nanocomposite VP-6h (figure 4 c), produced hydrothermally at 180 °C for 6 hours, has a semi-crystalline morphology characterized by spherical nanoclusters and a porous, agglomerated granular structure. The morphology, linked to homogeneous V_2O_5 dispersion and polaronic interactions, corresponds with EDX data indicating 60.49% C, 24.59% O, 12.87% N, and 2.04% V. The increased oxygen concentration (24.59%) and vanadium (2.04%) indicate partial preservation of the V_2O_5 structure in conjunction with PANI incorporation. In contrast, the VP-8h composite (figure 4 d), synthesized under the same circumstances but with an 8-hour reaction duration, demonstrates supplementary nanofiber development overlaid over porosity clusters. This structural development correlates with diminished electrical conductivity, presumably attributable to bipolaron formation and inadequate grain dispersion. EDX analysis for VP-8h reveals 61.88% carbon, 18.26% oxygen, 18.84% nitrogen, and 1.02% vanadium, demonstrating a significant reduction in oxygen and vanadium levels relative to VP-6h, coupled with an increase in nitrogen (18.84%), indicative of heightened PANI prevalence and suggesting accelerated PANI polymerization and vanadium reduction ($V^{5+} \rightarrow V^{4+}$) during prolonged reaction durations. These patterns validate XRD results, indicating that extended synthesis facilitates PANI intercalation, vanadium reduction, and phase transition, affecting the nanocomposite's electronic and morphological characteristics [40]. The reduction of vanadium and oxygen levels in VP-8h and nitrogen enrichment highlights the redox-mediated interaction between PANI and V_2O_5 during composite synthesis, essential for optimizing functional performance in sensing applications.

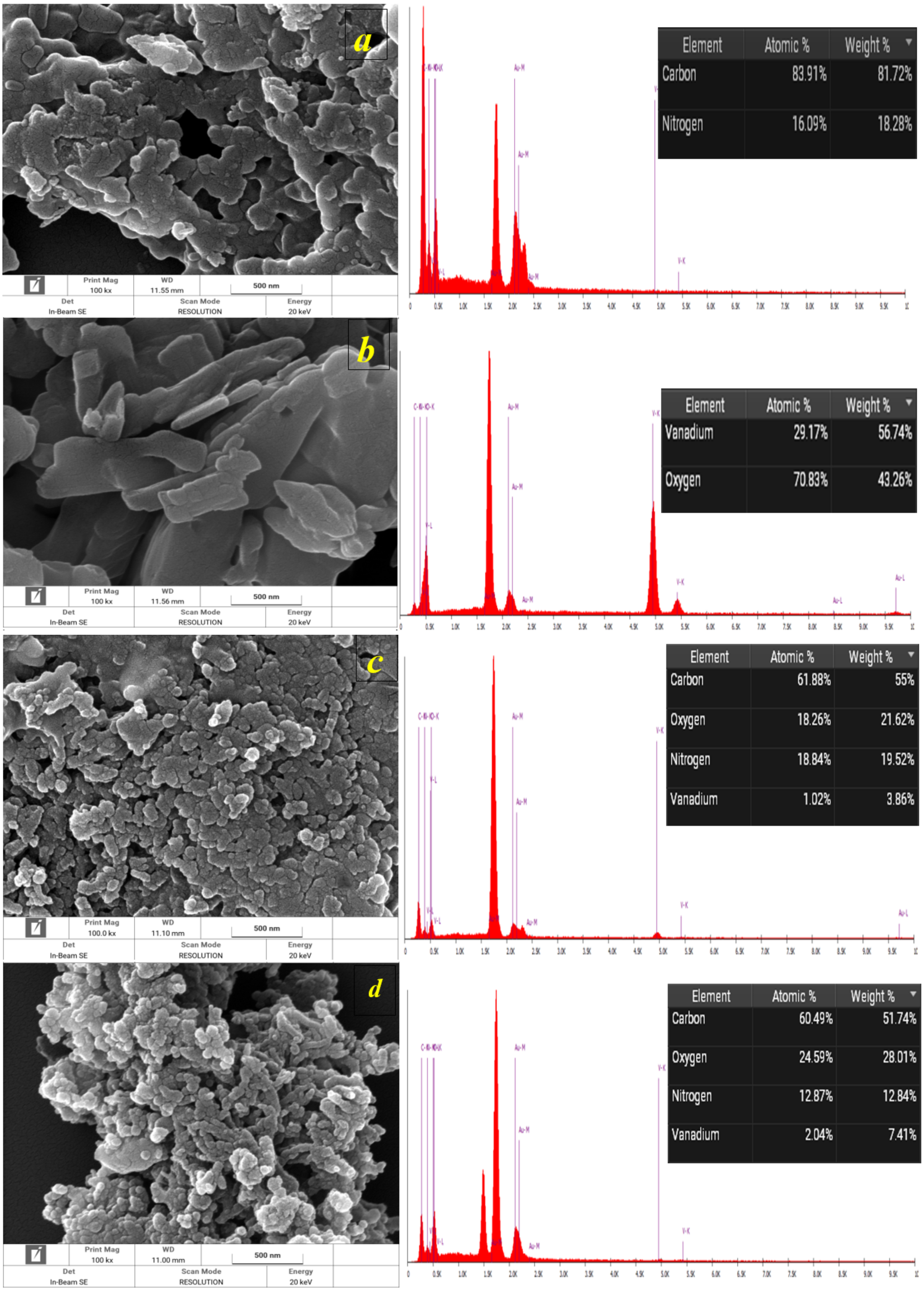

Element	Atomic %	Weight %
Carbon	83.91%	81.72%
Nitrogen	16.09%	18.28%

Element	Atomic %	Weight %
Vanadium	29.17%	56.74%
Oxygen	70.83%	43.26%

Element	Atomic %	Weight %
Carbon	61.88%	55%
Oxygen	18.26%	21.62%
Nitrogen	18.84%	19.52%
Vanadium	1.02%	3.86%

Element	Atomic %	Weight %
Carbon	60.49%	51.74%
Oxygen	24.59%	28.01%
Nitrogen	12.87%	12.84%
Vanadium	2.04%	7.41%

Figure 4. FESEM images and EDX spectra of (a) PANI (b) V_2O_5 (c) VP-6h and (d) VP-8h nanocomposite V_2O_5/PANI Synthesis with various reaction time 6h and 8h respectively.

3.4 Atomic Force Microscopy (AFM)

The 3D AFM micrographs and V_2O_5, PANI and V_2O_5/PANI histograms displayed in figure 5 (a) reveal a homogeneous rough high porosity surface morphology of PANI with RMS roughness 3.31375 nm, and the average particle size was 13.1465 nm. The rough, heterogeneous surface enhances the effective surface area, with the nanoparticle structure arising from the emeraldine salt form of polyaniline, which is semi-crystalline. The polymer's interwoven chains create porosity, indicating a semi-homogeneous distribution and possible voids or pores. Figure 5 (b) porosity-free morphology with homogeneity and uniformity on the sample surface of V_2O_5 pure was shown by the atomic force microscopy investigation. The surface of the film showed no signs of cracking. The grains' surface was covered in enormous, exquisitely divided conical columnar development, with some columnar grains clumping together in specific places. Its RMS roughness was 19.3263 nm, which was attributed to the polycrystalline structure of the film. Moreover, its average particle size was 101.843 nm. It should be mentioned that because rough surfaces have a significantly larger total surface area than smooth surfaces, significant sample roughness is necessary for photovoltaic applications [41]. The micrograph displays a uniform distribution of high-quality VP-6h particles with an average size of 32.8338 nm and RMS roughness (Sq) of 4.59369 nm at a reaction time of 6 hours figure 5 (c). The nanoparticles were observed to form spherical aggregates with a unique porosity. Nevertheless, the VP-8h prepared at a reaction time of 8 hours exhibited a distinct morphological feature. The VP-8h was observed to form as rough particles with irregular cylindrical shapes and an average size of 28.7720 nm and RMS roughness (Sq) of 4.60817 nm figure 5 (d). This is by the results of the FESEM. This result shows the substantial impact of reaction time on the hydrothermal process, suggesting that producing fine particles with a high surface area is feasible under shorter reaction periods.

3.5 Photoluminescence spectroscopy analysis

The photoluminescence (PL) spectra of PANI, V_2O_5, and nanocomposite samples (VP-6h and VP-8h) are displayed in figure 6. The excitation wavelength is 320 nm. As shown in figure 6 (a), four peaks of PANI may be attributable to a minimal difference in wavelength. A $\pi^* - \pi$ transition of the benzoic units and de-excitation from the polaron band was responsible for the genesis of the peak centered about 426 nm and 536 nm, respectively, as stated in reference [42]. Nothing is known about the source of the peak assigned to 608 nm. An association may be made between the bipolaron de-excitation and the faint peak at 724 nm. Additionally, the relative strength of the peak produced due to the de-excitation from the polaron band increases in proportion to the concentration of Hcl acid [43].

Additionally, the PL spectra of the V_2O_5 nanostructure can be seen due to four peaks. There are three peaks in the PL spectrum: around 414 nm, $501-580$ nm, and 752 nm. The band-edge transition of V_2O_5 is responsible for the significant peak that occurs around 580 nm. In comparison, the peak around 411 nm results from the transition from the top of the conduction band to the valance band of the material [44]. The extrinsic transition created by oxygen vacancies due to the annealing process is responsible for the emission that occurs at 752 nm [45].

As seen in figure 6 (b), the interaction between V_2O_5 and PANI resulted in the appearance of new peaks in the fundamental ranges of both materials and enhancements in the physical properties of each of the materials individually. It can be seen that the VP-8h has the look of on account of the $\pi - \pi^*$ transition of a benzenoid unit of PANI, the initial emission peak was seen at a wavelength of 351 nm [46]. The emission peak sites have demonstrated peak shifting, while the strength has steadily dropped with increasing excitation wavelength in VP-6h, which appears to have its peak at 386 nm. In samples, the peaks at 463 nm and 434 nm are present. A shift and a drop in intensity are seen in the VP-8h and VP-6h samples, respectively, when compared to the V_2O_5 and PANI samples [47]. The fact that it is connected with the polaron and bipolaron band transitions of PANI, respectively, suggests the interaction between PANI and V_2O_5. When conducting PANI, the charge carriers are essentially the polaron and the bipolaron. These interactions lead to the introduction of new electronic transitions and the rearranging of energy levels, both of which are not present in the materials in their natural state [48]. Because of this, electronic transit is improved, and the emission qualities are converted into something other. A range encompasses the third peak for VP-8h and VP-6h, as well as their respective peaks at 565 nm and 567 nm. The band-edge transition of V_2O_5 is responsible for the principal peak that can be found at around 580 nm [49]. This transition displays a slight change in intensity while retaining levels almost equal to those found in the pure sample of carbon dioxide. Sample VP-8h exhibits a shift and an increase in the intensity of the unknown peak at 660 nm, in contrast to the strength of the peak at 608 nm associated with pure PANI [50]. It is possible that the prolonged duration led to the formation of crystalline structural faults or distortions, in addition to interactions within the chain of the PANI molecule. As for the weak peaks that appear at $702-739$ nm in VP-8h and 762 nm in VP-6h, these peaks indicate the extrinsic transition created by oxygen vacancies as a result of the annealing process. In association with the bipolaron de-excitation, these faint peaks were seen. The relative strength of the peak that was formed owing to the de-excitation from the polaron band increases as the reaction time increases [51].

4. Photodetector characteristics

4.1 Current–voltage (I–V) characteristics

The current-voltage (I–V) characteristics of pure vanadium pentoxide (V_2O_5), polyaniline (PANI), and their hydrothermally synthesized nanocomposites (VP-6h and VP-8h) were assessed under dark and visible light circumstances with an illumination intensity of 10 mW/cm^2 at ambient temperature. The measurements were performed throughout a voltage range of -5 to $+5$ V, utilizing silver (Ag) as the electrode material, as seen in figure 7. The I–V characteristics of the pure devices demonstrate distinct rectifying

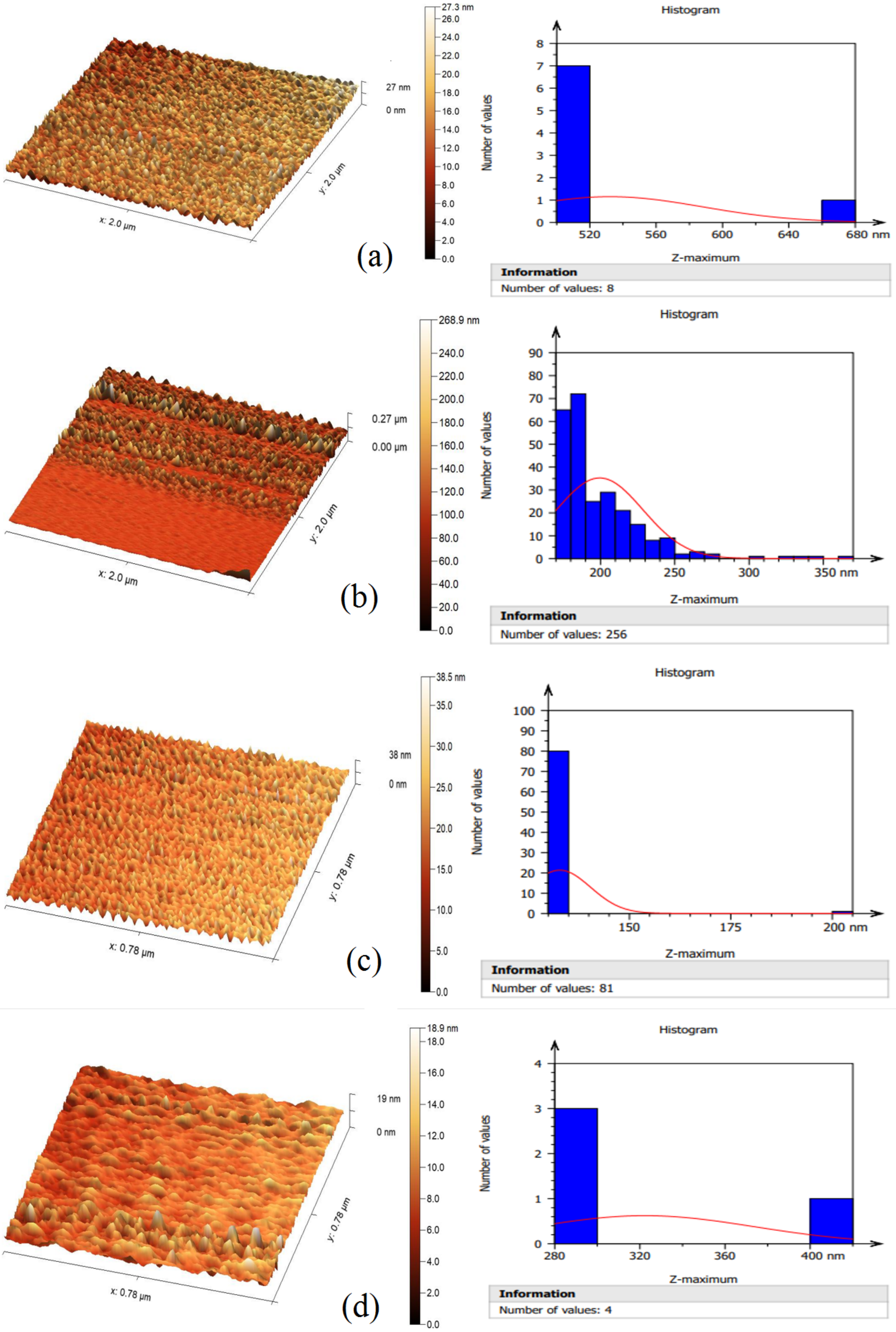

Figure 5. AFM 3-D images and histogram particles size of (a), PANI (b) V_2O_5 (c and d) V_2O_5/PANI NCPs synthesis with different reaction time 6h and 8h respectively.

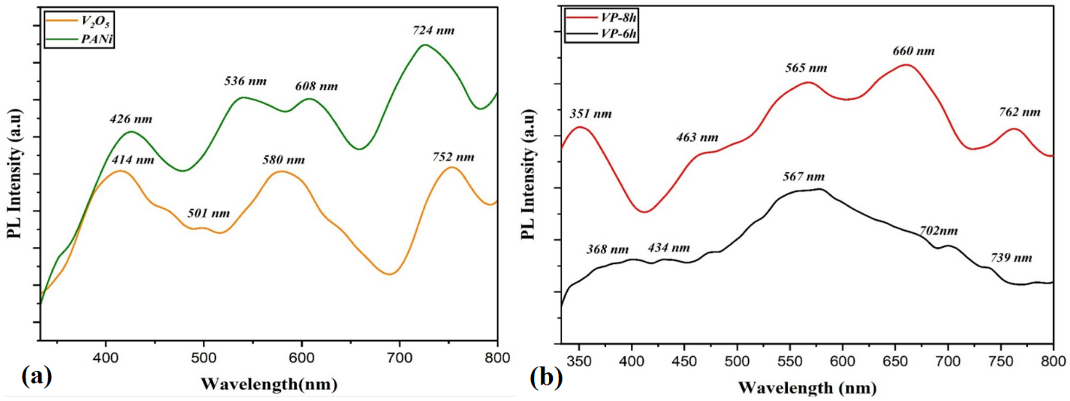

Figure 6. PL spectra of (a) V_2O_5 and PANI, (b) V_2O_5/PANI synthesized with different reaction time 6 hours (VP-6h) and 8 hours (VP-8h).

Table 2. Shows the bandgap energy of V_2O_5, PANI and V_2O_5/PANI NCPs.

Sample	Wavelength (nm)	Energy gap (eV)
V_2O_5	414,501,580 and 752	2.9,2.4,2.1 and 1.64
PANI	426,536,608 and 724	2.9,2.3,2.04 and 1.7
V_2O_5/PANI (6 h)	368,434,567 ,702 and 739	3.3,2.8,2.1,1.7 and 1.6
V_2O_5/PANI (8 h)	351,463,565,660 and 762	3.5,2.6,2.1,1.8 and 1.6

behavior and enhanced current under light, signifying photosensitivity. For V_2O_5, the photocurrent rose from 895.2 µA in darkness to 3543.4 µA under illumination at +5 V, but for PANI, it climbed from 816.8 µA to 3238.1 µA under the same circumstances. This improvement is due to the creation of electron-hole pairs when the energy of the incident photons surpasses the material's bandgap, and the relatively low dark current indicates a modest degree of dark noise. Nonetheless, these pure materials continue to experience restrictions in responsivity because of Schottky barriers and surface imperfections. The I-V behavior changes markedly when integrating V_2O_5 and PANI into nanocomposite structures via hydrothermal treatment. The VP-6h nanocomposite exhibited superior optoelectronic performance under

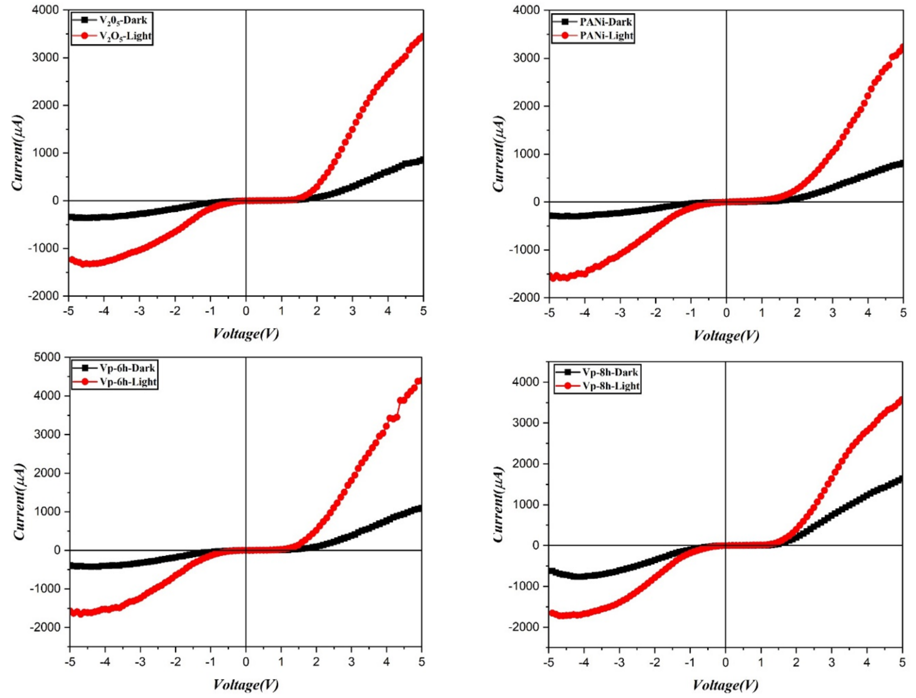

Figure 7. Current-voltage (I–V) characteristics of V_2O_5, PANI and the nanocomposite synthesized with different reaction time 6 hours (VP-6h) and 8 hours (VP-8h), respectively.

dark and illuminated conditions, as confirmed by current voltage (I–V) measurements. At ±5 V, VP-6h demonstrated significantly lower dark current values (387.4 µA at −5 V and 1099.2 µA at +5 V) compared to VP-8h (620.8 µA at −5 V and 1677.7 µA at +5 V), indicating reduced leakage current and minimal dark noise. This enhancement is primarily attributed to the improved crystallinity of VP-6h, as confirmed by X-ray diffraction (XRD) analysis, which correlates with a lower defect density and suppressed recombination of charge carriers. Furthermore, energy-dispersive X-ray spectroscopy (EDX) revealed a higher oxygen content in VP-6h, which facilitates electron trapping under dark conditions, contributing to the reduction of dark current [52]. Under illumination (10 mW/cm^2, visible light), VP-6h exhibited a significant increase in photocurrent, reaching 1571 µA at −5 V and 4395.6 µA at +5 V, which is considerably higher than that of VP-8h (1654.1 µA at −5 V and 3666.2 µA at +5 V). The enhanced photocurrent in VP-6h is attributed to the efficient separation of photogenerated electron-hole pairs at the V_2O_5/PANI heterojunction. Illumination leads to narrowing the depletion layer, which reduces the barrier for carrier transport, facilitating a higher current flow. Moreover, applying a reverse bias enhances the internal electric field, promoting more effective separation of carriers and boosting photocurrent. In contrast, the VP-8h sample, which underwent extended hydrothermal synthesis (8 h at 180 °C), displayed higher dark current and lower photocurrent enhancement. This degradation in performance is likely due to increased structural disorder and defect density, which act as recombination centers, thus limiting carrier mobility and overall device efficiency. Additionally, the role of surface-adsorbed oxygen species is evident during light exposure; photogenerated holes interact with adsorbed oxygen ions, leading to the desorption of O^- species and injection of electrons into the conduction band, thereby enhancing the photocurrent response [53]. These findings underscore the importance of optimized synthesis conditions in achieving nanocomposites with high photoresponsivity and low noise levels for photodetector applications.

4.2 Time-dependence characteristics

Photodetector behavior is influenced by key characteristics such as photo-switching and response/recovery time, which are critical for practical applications. As indicated in figure 8, The photo-switching behavior of the fabricated V_2O_5, PANI and nanocomposite (VP-6h, VP-8h) photodetectors was examined across multiple 10 mW/cm^2 illumination power cycles over three cycles of 10 s pulse with cycles at 2 bias voltages, indicating the device's durability and consistency. The apparatuses displayed the following response/recovery according. All four devices have excellent photoresponse, stability, and repeatability in each cycle. The current increased to the highest limit (light-ON) with an articulated response and diminished to its preliminary rate (light-OFF). The pure V_2O_5 device demonstrated a response and recovery time of 0.71 and 0.91 seconds, respectively, suggesting that the production rate of photogenerated electron-hole pairs is significantly quicker than the recombination rate. This characteristic is ascribed to the stratified orthorhombic configuration of V_2O_5, which provides elevated electron affinity and active surface spots that facilitate effective charge separation. Furthermore, terminal V=O bonds and inherent oxygen vacancies enhance electron mobility and reduce recombination. The comparatively porous structure and moderate surface roughness of the V_2O_5 layer promote light absorption and augment the effective surface area for carrier production, promoting better photoresponse efficiency.

Conversely, the pure PANI device exhibited extended response and recovery durations of 1.21/0.74 seconds. This indicates that the recombination rate exceeds the rate of electron-hole creation when illuminated. The reduced crystallinity, disordered molecular architecture, and restricted carrier mobility of PANI impede effective photocarrier production and transport. Moreover, the PANI film's comparatively smoother and denser surface, as seen by the AFM and FESEM pictures, leads to a diminished interfacial area and poorer light-matter interaction, constraining exciton dissociation and amplifying recombination losses [54].

The nanocomposite devices (VP-6h and VP-8h) demonstrated markedly enhanced response and recovery times of 0.62/0.59 s and 0.77/0.66 s, respectively. This improvement results from the synergistic interaction between the

Table 3. Represent the curent dark and light of V_2O_5, PANI and V_2O_5/PANI NCPs.

Photodetector device	Voltage (V)	Dark-Curent (µA)	Light-Curent (µA)
V_2O_5	+5	870	3543.4
	−5	339.1	1236.4
PANI	+5	816.8	3238.08
	−5	284.6	1535
VP-6h	+5	1099.2	4395.6
	−5	387.4	1571
VP-8h	+5	1643	3666.2
	−5	620.8	1654.1

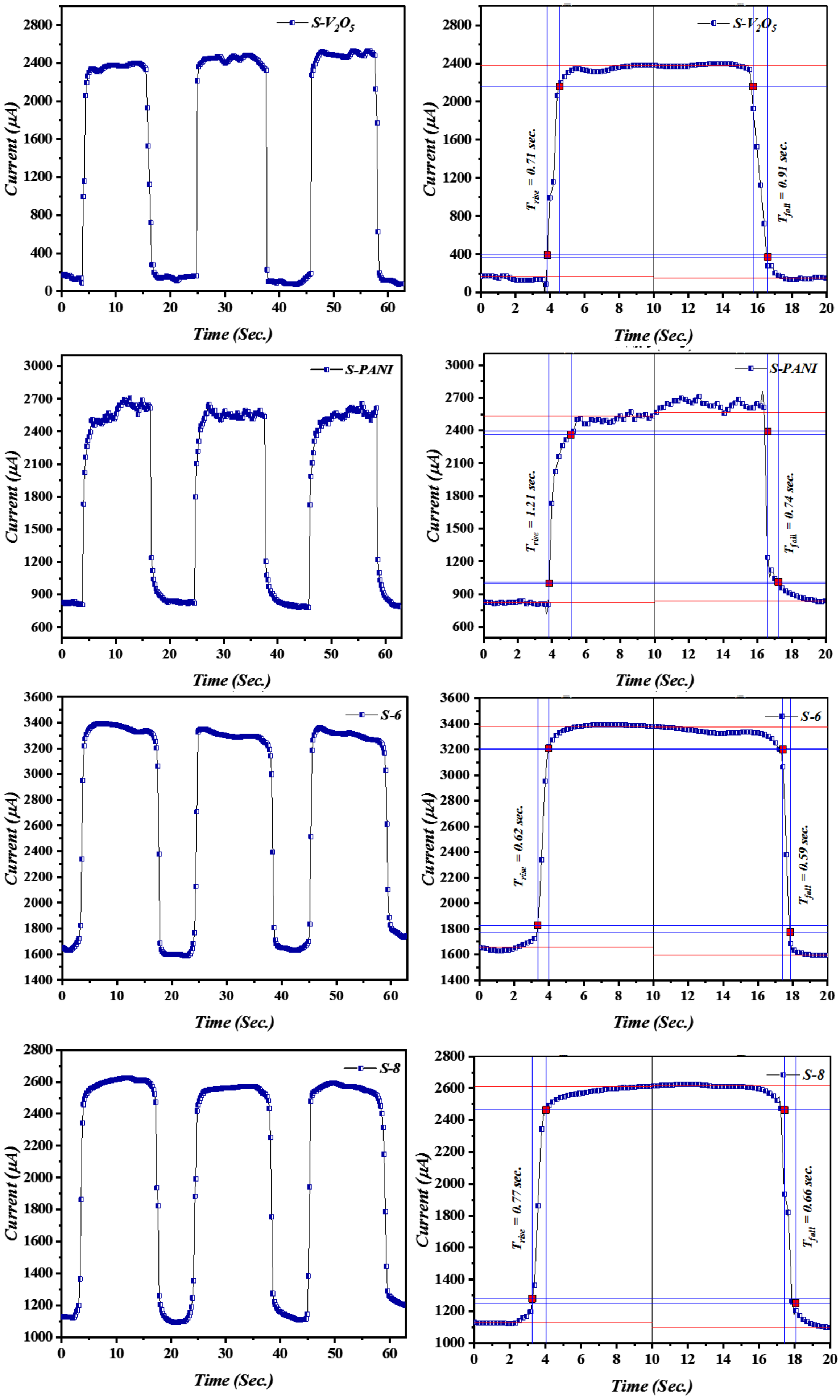

Figure 8. Time-resolved characteristics of V_2O_5, PANI and the nanocomposite synthesized with different reaction time 6 hours (VP-6h) and 8 hours (VP-8h), respectively.

inorganic V_2O_5 phase and the organic PANI matrix. The hybrid structure leverages the elevated carrier mobility of V_2O_5 and PANI's flexible, conductive framework, facilitating rapid separation and extraction of photogenerated carriers. The nanocomposite films have enhanced surface roughness and porosity, as AFM and FESEM investigations show [55, 56]. These textural characteristics augment light scattering and absorption, offering more active charge separation and transport sites. The coarse, porous texture enhances the interfacial contact area between the two phases, promoting interfacial charge transfer and diminishing the likelihood of recombination. Interestingly, different reaction times for nanocomposites result in varying conductivities, which contribute to diverse photovoltaic performance. This phenomenon indicates a rapid electron injection and relatively slow electron/hole recombination in the hybrid system [57].

4.3 Spectral dependency

Figure 9 illustrates the principal performance parameters of the photodetector, encompassing responsivity, detectivity, and external quantum efficiency (EQE) throughout an extensive spectrum range of 300 to 850 nm. This wavelength range encompasses the ultraviolet (UV), visible, and near-infrared (NIR) ranges, enabling a thorough assessment of the device's optoelectronic response. Spectral dependency (R_λ) is a crucial parameter for assessing photodetector performance, as it measures the device's sensitivity to various wavelengths of incident light and can be computed using the equation.

$$R_\lambda = \frac{I_{\text{ph}}}{P_{\text{light}}} \tag{5}$$

where I_{ph} is the output photocurrent and P_{light} is the amount of incident illumination power [58]. Moreover, if the DC shot noise is the primary source of the produced noise, the photodetectivity (D^*), which is determined using equation (2), is another essential metric for estimating a photodetector's performance [59].

$$D^* = \frac{R_\lambda}{\sqrt{2qI_D}} \tag{6}$$

Here, q and I_D stand for the electron charge (1.6×10^{-19} C) and dark current, respectively. And to further quantify this gain, we measured the EQE of the PDs in reaction to light. EQE is an important measure for quantifying PD behavior and may be calculated as follows [60].

$$\text{EQE} = \frac{R_\lambda \times h \times c}{q \times \lambda} \times 100\% \tag{7}$$

where h is the Planck's constant, c is the light velocity, q is the electron charge, λ is the incoming light wavelength, and R_λ is the responsivity at the wavelength of λ nm. The spectral response of the fabricated photodetectors, illustrated in figure 9 (a–c), was examined under an illumination power of 10 mW/cm^2 at 2 bias voltage, demonstrating moderate sensitivity in the UV region and a notable increase in R_λ, D^*, and EQE values at visible wavelengths, especially between 450 nm and 600 nm, which aligns with the optical

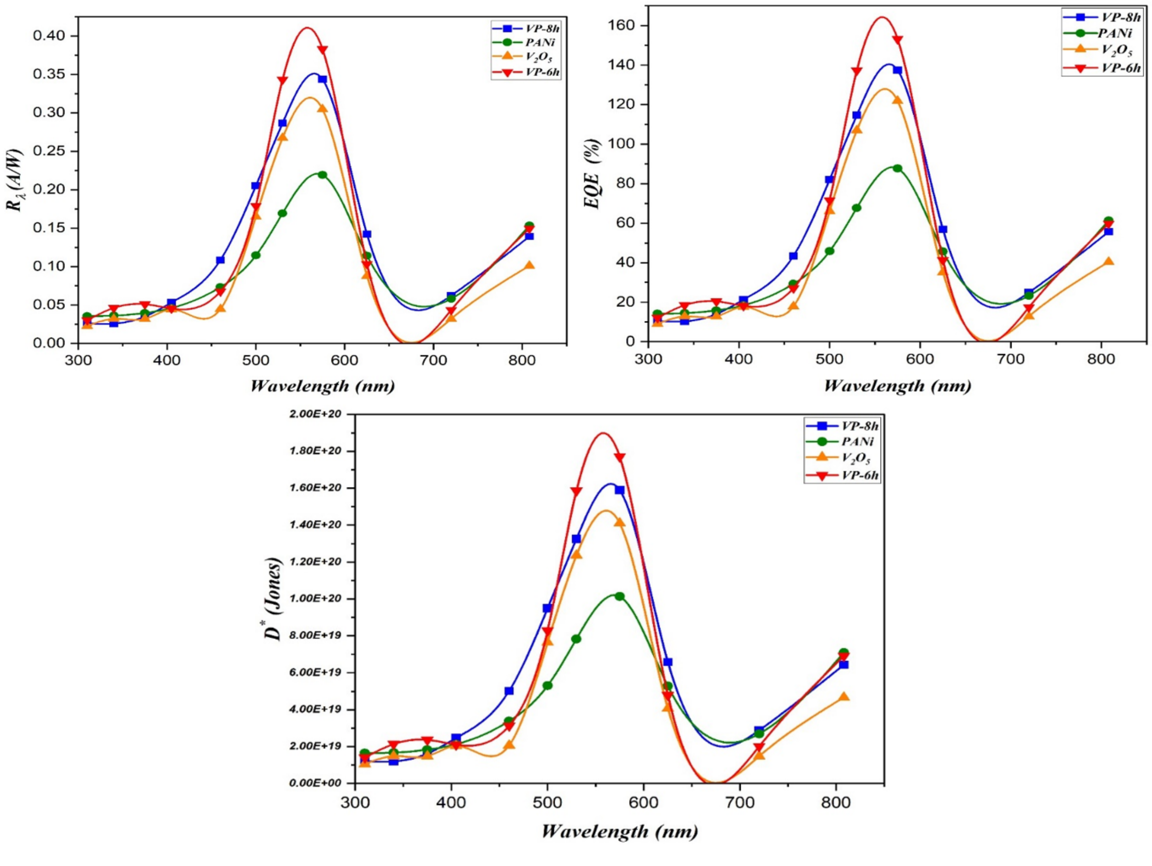

Figure 9. Photodetector responsivity, detectivity, and external quantum for PANI, V_2O_5, and V_2O_5/PANI nanocomposite synthesized with 6h (VP-6h) and 8h (VP-8h) reaction times, efficiency, respectively.

Table 4. Shows responsivity, detectivity external quantum efficency and recovery time.

Photodetector device	$R(\lambda)$	$D^* \times 10^{20}$	EQE	REC-Time
V_2O_5	0.304	1.41	121.96	0.71/0.91
PANI	0.219	1.01	87.68	1.21/0.74
VP-6h	0.383	1.77	153.2	0.62/0.59
VP-8h	0.343	1.59	137.52	0.77/0.66

bandgap analysis. A quantifiable reaction at wavelengths greater than 700 nm may indicate sub-bandgap transitions, maybe attributable to defect states or surface plasmonic effects caused by the hybrid nanostructures. The hybrid photodetector VP-6h, synthesized by 6 hours of hydrothermal treatment, had all investigated devices' greatest performance metrics (R_λ, D^*, EQE), indicating its optimized crystalline structure and enhanced charge transport dynamics. In contrast, VP-8h, synthesized over 8 hours, exhibited intermediate values surpassing those of the unaltered V_2O_5 and PANI devices but inferior to VP-6h suggesting that extended reaction time may elevate structural flaws, thereby reducing carrier mobility. The results collectively indicate that the pronounced photoresponsivity and detectivity in the hybrid devices arise not solely from the mesoporous morphology but are also substantially affected by particular nanostructures characteristics, including V_2O_5 nanowires and platelets, which augment charge separation and current density, underscoring the significance of precise nanostructure fabrication in optimizing photodetector performance.

4.4 Photodetector mechanism of devices

The photo-response of V_2O_5/PANI nanocomposites (VP-6h, VP-8h) under visible light illumination and a 2 V applied bias results from synergistic charge transport kinetics and interfacial band engineering. The polaron lattice structure in PANI facilitates effective intra- and inter-chain hopping of delocalized $\pi-$electrons and holes, producing free photo-excitons inside its intermediate gap states via the aggregation of radical cations [14, 61]. Simultaneously, visible light irradiation stimulates electron-hole pairs in the mixed nanorod/nanosheet structure of V_2O_5, which are segregated by the intrinsic electric field at the V_2O_5/PANI interface. Photo-generated holes traverse the V_2O_5 valence band and transition to the HOMO level of PANI. At the same time, electrons are elevated to the conduction band of V_2O_5, aided by a cascade band-edge alignment (1.6 eV) that connects the LUMO of PANI with the conduction band of V_2O_5 figure 10 (c) [61]. The implemented bias expedites this process, amplifying carrier drift and reducing recombination. PANI serves as a conductive conduit,

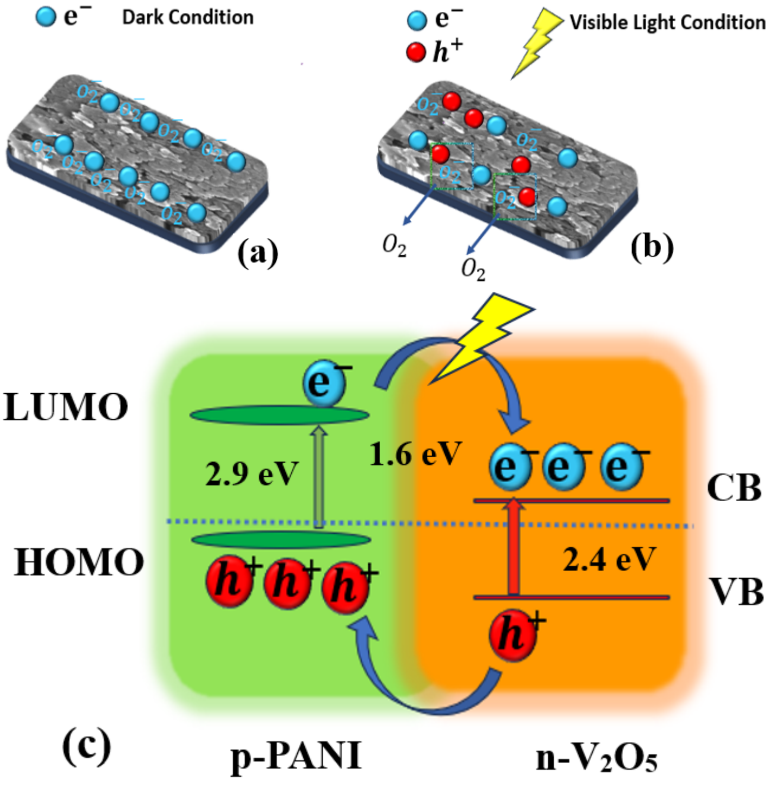

Figure 10. Illustrative schematic diagram of V_2O_5/PANI in (a) dark and (b) light conditions (c) schematic energy band diagram of the V_2O_5/PANI heterojunction.

enhancing photocurrent through polaron-mediated exciton generation. At the same time, figure 10 (a,b) illustrates adsorbed oxygen species on V_2O_5/VO_2 surfaces regulate depletion layers: upon illumination, trapped holes desorb oxygen $h^+ + O_2^-$ (ad) $\rightarrow O_2$ (g) diminishing barrier height and thickness, thus facilitating the occupation of unpaired electrons in the conduction band and increasing conductivity [52]. Following light removal, recombination through bipolaron states in PANI swiftly reinstates the dark current. In contrast, the restricted grains of V_2O_5 and the intermediate gap states of PANI guarantee stable on/off current ratios throughout cycles. The rectifying I-V characteristics and persistent photoresponse across different light intensities (Fig. 10) underscore the essential functions of interfacial charge separation, polaron dynamics, and bias-enhanced transport in attaining adjustable optoelectronic performance, differentiating this mechanism from self-powered systems that depend exclusively on built-in potentials.

5. Conclusion

A series of photodetectors employing pure V_2O_5, PANI, and hydrothermally produced V_2O_5/PANI nanocomposites (VP-6h and VP-8h) were effectively constructed by spray coating on silicon substrates. XRD analysis verified the existence of orthorhombic V_2O_5 and identified monoclinic VO_2 phases in the nanocomposites, demonstrating successful phase integration. FESEM and AFM analyses revealed that VP-6h exhibited a highly porous morphology and excellent surface roughness, conducive to improved photodetection, whereas VP-8h displayed nanorod production. Raman spectroscopy confirmed the practical synthesis by detecting distinctive vibrational modes of each component. Photoluminescence investigations established the detector's active spectral range as 450 to 650 nm, aligning with the high responsivity (0.383 A/W), detectivity (1.77×10^{20} Jones), and external quantum efficiency (153.2%) demonstrated by VP-6h under a 2 V bias and 10 mW/cm^2 illumination. Moreover, rapid response and recovery periods further illustrate its appropriateness for practical applications. The present research emphasizes the innovative application of hydrothermally produced V_2O_5/PANI nanocomposites with customized shape and phase composition, leading to markedly enhanced photodetector performance. These findings provide significant insights for developing sophisticated, economical hybrid optoelectronic devices.

Authors Contribution
The intellectual substance, idea, and design of this study, or the analysis and interpretation of the data (if applicable), as well as the manuscript's writing, were all sufficiently contributed to by each author.

Availability of data and materials
The data that support the findings of this study are available from the corresponding author upon reasonable request.

Conflict of interests
The authors declare that they have no known competing financial interests or personal relationships that could have appeared to influence the work reported in this paper.

References

[1] R. Tamang, B. Varghese, E. S. Tok, S. Mhaisalkar, and C. H. Sow. "Sub-bandgap energy photoresponse of individual V_2O_5 nanowires.". *Nanoscience and Nanotechnology Letters*, **4**(7):716–719, 2012.

[2] B. H. Kim, A. Kim, S.-Y. Oh, S.-S. Bae, Y. J. Yun, and H. Y. Yu. "Energy gap modulation in V_2O_5 nanowires by gas adsorption.". *Applied Physics Letters*, **93**(23), 2008.

[3] B. Priya, P. J. Arunima, and T. Kumar. "Structural, morphological and optical properties of V_2O_5 thin films.". *Growth And Characterization Of Semiconductor Nanostructure For Device Applications*, page 106, 2023.

[4] S. Xun et al. "Ionic liquid promotes high dispersion of V_2O_5 on 3D porous g-C_3N_4 carrier to enhance catalytic oxidative desulfurization performance.". *Energy & Fuels*, **37**(8):6276–6280, 2023.

[5] V. Modafferi, S. Trocino, A. Donato, G. Panzera, and G. Neri. "Electrospun V_2O_5 composite fibers: synthesis, characterization and ammonia sensing properties.". *Thin Solid Films*, **548**:689–694, 2013.

[6] H. Rahman, H. Dhoundiyal, A. Kumar, and M. C. Bhatnagar. "Fabrication and electrical surface characterization of pellets of V_2O_5 nanostructures for robust and portable gas sensor applications.". *Applied Physics A*, **129**(4):271, 2023.

[7] A. S. Altowyan, J. Hakami, H. Algarni, and M. Shkir. "Enhancing the optoelectronic properties of V_2O_5 thin films through Tb doping for photodetector applications.". *Journal of Alloys and Compounds*, **960**:170911, 2023.

[8] R. Madaka et al. "Two-dimensional transition metal oxides (TMOs) for solar cell applications. In: Two-dimensional Hybrid Composites: Synthesis, Properties and Applications.". Springer:53–86, 2024.

[9] W. Ouyang, F. Teng, J. H. He, and X. Fang. "Enhancing the photoelectric performance of photodetectors based on metal oxide semiconductors by charge-carrier engineering.". *Advanced Functional Materials*, **29**(9):1807672, 2019.

[10] M. Lira-Cantú and P. Gómez-Romero. "Multifunctional hybrid materials based on conducting organic polymers. Nanocomposite systems with photo-electro-ionic properties and applications. In: Functional hybrid materials.". Wiley-VCH Verlag GmbH & Co. KGaA, 2004.

[11] H. Kumar, A. Boora, and A. Yadav. "Polyaniline-metal oxide-nanocomposite as a nano-electronics, opto-electronics, heat resistance and anticorrosive material.". *Results in Chemistry*, **2**:100046, 2020.

[12] B. Guo, G. Wu, H.-Z. Chen, and M. Wang. "Solution-processed organic/inorganic hybrid photodetector with selective deep UV sensitivity.". *Organic Electronics*, **29**:13–21, 2016.

[13] T. Sen, S. Mishra, and N. G. Shimpi. "Synthesis and sensing applications of polyaniline nanocomposites: A review.". *RSC advances*, **6**(48):42196–42222, 2016.

[14] S. Bhadra, N. K. Singha, and D. Khastgir. "Polyaniline by new miniemulsion polymerization and the effect of reducing agent on conductivity.". *Synthetic Metals*, **156**(16-17):1148–1154, 2006.

[15] S. Banerjee and A. Kumar. "Swift heavy ion irradiation induced modifications in the optical band gap and Urbach's tail in polyaniline nanofibers.". *Nuclear Instruments and Methods in Physics Research Section B: Beam Interactions with Materials and Atoms*, **269**(23): 2798–2806, 2011.

[16] M. M. Mahdi, E. T. Salim, and A. S. J. M. T. C. Obaid. "Au@ Nb_2O_5 core/porous-shell nanoparticles: Synthesis and characterization at different laser pulse.". page 112719, 2025.

[17] K. Shafeeq, V. Athira, C. R. Kishor, and P. Aneesh. "Structural and optical properties of V_2O_5 nanostructures grown by thermal decomposition technique.". *Applied Physics A*, **126**:1–6, 2020.

[18] B. S. Singu, P. Srinivasan, and S. Pabba. “Benzoyl peroxide oxidation route to nano form polyaniline salt containing dual dopants for pseudocapacitor.”. *Journal of The Electrochemical Society*, **159**(1): A6, 2011.

[19] D. Sutar, N. Padma, D. Aswal, S. Deshpande, S. Gupta, and J. Yakhmi. “Preparation of nanofibrous polyaniline films and their application as ammonia gas sensor.”. *Sensors and Actuators B: Chemical*, **128**(1):286–292, 2007.

[20] S. Kundu, B. Satpati, T. Kar, and S. K. Pradhan. “Microstructure characterization of hydrothermally synthesized PANI/$V_2O_5 \cdot nH_2O$ heterojunction photocatalyst for visible light induced photodegradation of organic pollutants and non-absorbing colorless molecules.”. *Journal of Hazardous Materials*, **339**:161–173, 2017.

[21] J. Lemerle, L. Nejem, and J. Lefebvre. “Condensation process in polyvanadic acid solutions.”. *Journal of Inorganic and Nuclear Chemistry*, **42**(1):17–20, 1980.

[22] M. M. Mahdi, A. M. Ali, M. A. Alalousi, D. A. Kadhim, and M. A. J. V. Abid. “Developing a copper-zinc-aluminum alloying technique by vacuum thermal deposition after irradiation by gamma rays (NaI (Ti)) with stabilized zinc metal.”. **219**:112676, 2024.

[23] F. Smith. “Industrial applications of X-ray diffraction.”. CRC press, 1999.

[24] A. Viswanathan and A. N. Shetty. “Influence of different dopants and redox forms of PANI in its crystal structure, morphology, electrochemical energy storage to variable extent, unique properties and kinetics.”. *Bulletin of Materials Science*, **45**(2):60, 2022.

[25] D. Mukherjee et al. “Evaluation of temperature-dependent microstructural and nanomechanical properties of phase pure V_2O_5.”. *Journal of Sol-Gel Science and Technology*, **87**:347–361, 2018.

[26] A. Baltakesmez, C. Aykaç, and B. Güzeldir. “Phase transition and changing properties of nanostructured V_2O_5 thin films deposited by spray pyrolysis technique, as a function of tungsten dopant.”. *Applied Physics A*, **125**:1–18, 2019.

[27] A. Parija, Y. Liang, J. L. Andrews, L. R. De Jesus, D. Prendergast, and S. Banerjee. “Topochemically de-intercalated phases of V_2O_5 as cathode materials for multivalent intercalation batteries: A first-principles evaluation.”. *Chemistry of Materials*, **28**(16):5611–5620, 2016.

[28] P. Shvets, K. Maksimova, and A. Goikhman. “In situ XRD and Raman study of the phase transition in V_2O_5 xerogels.”. *Journal of Non-Crystalline Solids*, **625**:122751, 2024.

[29] W. Ji. “Characterization of vanadium, manganese and iron model clusters by vibrational and optical spectroscopic methods. ”. University of Houston, 1999.

[30] D. Li, J. Huang, and R. B. Kaner. “Polyaniline nanofibers: a unique polymer nanostructure for versatile applications.”. *Accounts of Chemical Research*, **42**(1):135–145, 2009.

[31] G. M. do Nascimento and M. A. de Souza. “Spectroscopy of nanostructured conducting polymers.”. *Nanostructured Conductive Polymers*, pages 341–373, 2010.

[32] H. S. Abdullah. “Electrochemical polymerization and Raman study of polypyrrole and polyaniline thin films.”. *Int J Phys Sci*, **7**(38): 5468–5476, 2012.

[33] M. M. Nobrega, M. Ceppatelli, M. L. Temperini, and R. Bini. “Pressure-induced reactivity in the emeraldine salt and base forms of polyaniline probed by FTIR and Raman.”. *Journal of Physical Chemistry C*, **118**(47):27559–27566, 2014.

[34] M. Marezio, D. B. McWhan, J. Remeika, and P. Dernier. “tructural Aspects of the Metal-Insulator Transitions in Cr-Doped VO_2.”. *Physical Review B*, **5**(7):2541, 1972.

[35] B. Akyürek. “Electrical Characterization of Vanadium Dioxide (VO_2) Thin Films Grown by Magnetron Sputtering Technique.”. *Izmir Institute of Technology (Turkey)*, 2024.

[36] A. Roy, A. Ray, P. Sadhukhan, S. Saha, and S. Das. “Morphological behaviour, electronic bond formation and electrochemical performance study of V_2O_5-polyaniline composite and its application in asymmetric supercapacitor.”. *Materials Research Bulletin*, **107**:379–390, 2018.

[37] S. Li, T. Zhou, Y. Cheng, and X. Li. “Preparation of V_2O_5 Composite Cathode Material Based on In-Situ Intercalated Polyaniline and Its High-Performance Aqueous Zinc-Ion Battery Applications.”. 2025.

[38] K. D. Alanazi, B. H. Alshammari, R. Bashir, and S. U. Asif. “Fabrication and characterization of vanadium oxide-polyaniline (VOP) composites for high-performance supercapacitors.”. *Journal of Sol-Gel Science and Technology*, **110**:291–303, 2024.

[39] S. Ashraf and S. Islam. “Synthesis and characterization of polyaniline (PANI) doped with vanadium pentoxide (V_2O_5).”. *Digest Journal of Nanomaterials & Biostructures (DJNB)*, **15**(3), 2020.

[40] C.-G. Wu et al. “Redox intercalative polymerization of aniline in V_2O_5 xerogel. The postintercalative intralamellar polymer growth in polyaniline/metal oxide nanocomposites is facilitated by molecular oxygen.”. *Chemistry of Materials*, **8**(8):1992–2004, 1996.

[41] T.-C. Lin, B.-J. Jheng, H.-M. Yen, and W.-C. Huang. “Thermal annealing effects of V_2O_5 thin film as an ionic storage layer for electrochromic application.”. *Materials*, **15**(13):4598, 2022.

[42] A. El-Naggar et al. “Exploring the structural, optical and electrical characteristics of PVA/PANi blends.”. *Optical Materials*, **139**: 113771, 2008.

[43] S. Banerjee, S. Sarmah, and A. Kumar. “Photoluminescence studies in HCl-doped polyaniline nanofibers.”. *Journal of Optics*, **38**:124–130, 2009.

[44] C. Lamsal and N. Ravindra. “Optical properties of vanadium oxides-an analysis.”. *Journal of Materials Science*, **48**:6341–6351, 2013.

[45] M. Kang, M. Chu, S. W. Kim, and J.-W. Ryu. “Optical and electrical properties of V_2O_5 nanorod films grown using an electron beam.”. *Thin Solid Films*, **547**:198–201, 2013.

[46] M. Beygisangchin, S. Abdul Rashid, S. Shafie, and A. R. Sadrolhosseini. “Polyaniline synthesized by different dopants for fluorene detection via photoluminescence spectroscopy.”. *Materials*, **14**(23): 7382, 2021.

[47] L. T. B. Mendonça, A. G. Bezerra Jr, and W. M. de Azevedo. “Preparation and characterization of V_2O_5 and V_2O_5/PANI nanocomposite by laser ablation technique in liquid.”. *Materials Chemistry and Physics*, **273**:125084, 2021.

[48] A. B. Rohom, P. U. Londhe, and N. B. Chaure. “Oxidative Polymerization of Polyaniline (PANI) Colloids with Different Oxidizing Agents.”. *ECS Journal of Solid State Science and Technology*, **10**: 081013, 2021.

[49] A. K. Kumawat, S. S. Rathore, S. Singh, and R. Nathawat. “Structural transition and photoluminescence behavior of (V_2O_5) 1-x (Ag0. 33V_2O_5) x (x = 0 to 0.1) nanocomposites.”. *Results in Chemistry*, **5**: 100802, 2023.

[50] V. S. R. Channu, R. Holze, B. Rambabu, and R. R. Kalluru. “Synthesis and characterization of PANI nanostructures for supercapacitors and photoluminescence.”. *Iranian Polymer Journal*, **21**:457–462, 2012.

[51] A. B. Rohom, P. U. Londhe, S. Mahapatra, S. Kulkarni, and N. Chaure. “Electropolymerization of polyaniline thin films.”. *High Performance Polymers*, **26**(6):641–646, 2014.

[52] Z. Wang et al. “Transferable and flexible nanorod-assembled TiO_2 cloths for dye-sensitized solar cells, photodetectors, and photocatalysts.”. *ACS nano*, **5**(10):8412–8419, 2011.

[53] M. B. A. Bashir, E. Y. Salih, A. H. Rajpar, G. Bahmanrokh, and M. F. M. Sabri. “he impact of laser energy on the photoresponsive characteristics of CdO/Si visible light photodetector.”. *Journal of Micromechanics and Microengineering*, **32**(8):085006, 2022.

[54] A. Qadir et al. “Recent advancements in polymer-based photodetector: A comprehensive review.”. *Sensors and Actuators A: Physical*, page 115267, 2024.

[55] S. Hinds, L. Levina, E. J. Klem, G. Konstantatos, V. Sukhovatkin, and E. H. Sargent. “Smooth-morphology ultrasensitive solution-processed photodetectors.”. *Adv. Mater*, **20**(23):4398–4402, 2008.

[56] B. M. Alotaibi, H. A. Al-Yousef, N. A. Alsaif, and A. Atta. “Characterization and optical properties of polymer nanocomposite films for optoelectronic applications.”. *Surface Innovations*, **11**(1-3):142–154, 2022.

[57] X. Shi, M. Fujitsuka, S. Kim, and T. Majima. “Faster electron injection and more active sites for efficient photocatalytic H_2 evolution in g-C_3N_4/MoS_2 hybrid.”. *Small*, **14**:1703277, 2018.

[58] E. Y. Salih et al. “Preparation and characterization of ZnO/$ZnAl_2O_4$-mixed metal oxides for dye-sensitized photodetector using Zn/Al-layered double hydroxide as precursor.”. *Journal of Nanoparticle Research*, **21**, pages = 1-12, year = 2019.

[59] E. Y. Salih, M. B. A. Bashir, A. H. Rajpar, I. A. Badruddin, and G. Bahmanrokh. “Rapid fabrication of NiO/porous Si film for ultraviolate photodetector: The effect of laser energy.”. *Microelectronic Engineering*, **258**:111758, 2022.

[60] M. M. Mahdi, E. T. Salim, and A. S. J. P. Obaid. “A Comparison Study of Au@ Nb_2O_5 Core–Shell Nanoparticle Using Two Different Laser Flounces.”. pages 1–14, 2025.

[61] S. Yang, X. Cui, J. Gong, and Y. Deng. “Synthesis of TiO_2–polyaniline core–shell nanofibers and their unique UV photoresponse based on different photoconductive mechanisms in oxygen and non-oxygen environments.”. *Chemical Communications*, **49**: 4676–4678, 2013.